JOURNAL OF APPLIED PHYSICS **110**, 114305 (2011)

Excitation of discrete and continuous spectrum for a surface conductivity model of graphene

George W. Hanson,[1] Alexander B. Yakovlev,[2] and Arash Mafi[1]
[1]*Department of Electrical Engineering, University of Wisconsin-Milwaukee 3200 N. Cramer St., Milwaukee, Wisconsin 53211, USA*
[2]*Department of Electrical Engineering, The University of Mississippi University, Mississippi 38677, USA*

(Received 2 September 2011; accepted 20 October 2011; published online 1 December 2011)

Excitation of the discrete (surface-wave/plasmon propagation mode) and continuous (radiation modes) spectrum by a point current source in the vicinity of graphene is examined. The graphene is represented by an infinitesimally thin, local, and isotropic two-sided conductivity surface. The dynamic electric field due to the point source is obtained by complex-plane analysis of Sommerfeld integrals, and is decomposed into physically relevant contributions. Frequencies considered are in the GHz through mid-THz range. As expected, the TM discrete surface wave (surface plasmon) can dominate the response along the graphene layer, although this depends on the source and observation point location and frequency. In particular, the TM discrete mode can provide the strongest contribution to the total electric field in the upper GHz and low THz range, where the surface conductivity is dominated by its imaginary part and the graphene acts as a reactive (inductive) sheet.
 [doi:10.1063/1.3662883]

I. INTRODUCTION

Graphene is a promising material for a range of electronic and electromagnetic applications.[1–3] Recently, graphene samples with large lateral dimensions have been fabricated,[4,5] allowing for plasmonic applications in the far through near infrared range of frequencies. Plasmonic and waveguiding properties of graphene have been considered in a number of previous studies; some basic plasmonic properties of graphene have been presented in Refs. 6–11, and graphene applications as THz plasmon oscillators,[12] tunable waveguiding interconnects,[13] surface plasmon modulators,[14] pn junctions,[15] and basic waveguiding structures and interconnects[16–20] have been examined.

In this work, the interaction of a point source and an infinite graphene sheet is considered. The electromagnetic fields are governed by classical Maxwell's equations, and the graphene is represented by a conductivity surface arising from a semiclassical (intraband) and quantum-dynamical (interband) model. For the given impedance surface model, the electromagnetic solution is exact. The electric field is expressed in terms of three contributions: the direct field radiated by the source in the absence of the graphene surface (i.e., the "line-of-sight" contribution), the discrete (residue) surface-wave mode, and the continuous (branch cut) radiation mode spectrum. For applications, the discrete mode is of primary importance, and here emphasis is placed on exciting the discrete mode using a vertical point source. It is shown that the discrete plasmon mode can be strongly excited and confined near the graphene surface in the low THz range. In the following all units are in the SI system, and the time variation (suppressed) is $e^{j\omega t}$, where j is the imaginary unit.

II. FORMULATION OF THE MODEL

A. Graphene as a two-sided impedance surface

Figure 1 depicts laterally infinite graphene having conductivity σ (S) lying in the x-z plane at the interface between two different mediums characterized by μ_1, ε_1 for $y>0$ and μ_2, ε_2 for $y<0$, where all material parameters may be complex valued.

The graphene is modeled as an infinitesimally thin, local, two-sided surface characterized by a surface conductivity $\sigma(\omega,\mu_c,\Gamma,T)$, where ω is radian frequency, μ_c is chemical potential, Γ is a phenomenological scattering rate that is assumed to be independent of energy ε, and T is temperature. For the conductivity of graphene we use the expression resulting from the Kubo formula,[21]

$$\sigma(\omega,\mu_c,\Gamma,T)=\frac{je^2(\omega-j\Gamma)}{\pi\hbar^2}\times\left[\frac{1}{(\omega-j\Gamma)^2}\int_0^\infty \varepsilon\left(\frac{\partial f_d(\varepsilon)}{\partial\varepsilon}-\frac{\partial f_d(-\varepsilon)}{\partial\varepsilon}\right)d\varepsilon-\int_0^\infty\frac{f_d(-\varepsilon)-f_d(\varepsilon)}{(\omega-j\Gamma)^2-4(\varepsilon/\hbar)^2}d\varepsilon\right], \tag{1}$$

where e is the charge of an electron, $\hbar=h/2\pi$ is the reduced Planck's constant, $f_d(\varepsilon)=\left(e^{(\varepsilon-\mu_c)/k_BT}+1\right)^{-1}$ is the Fermi-Dirac distribution, and k_B is Boltzmann's constant. We assume that no external magnetic field is present, and so the local conductivity is isotropic (i.e., there is no Hall conductivity).

The first term in Eq. (1) is due to intraband contributions, and the second term to interband contributions. The intraband term in Eq. (1) can be evaluated as

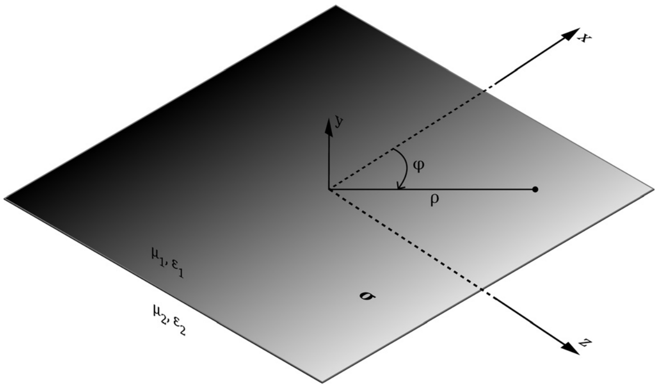

FIG. 1. Graphene characterized by surface conductivity σ at the interface between two dielectrics.

$$\sigma_{\text{intra}}(\omega,\mu_c,\Gamma,T) = -j\frac{e^2 k_B T}{\pi\hbar^2(\omega - j\Gamma)}\left(\frac{\mu_c}{k_B T} + 2\ln\left(e^{\frac{-\mu_c}{k_B T}} + 1\right)\right). \tag{2}$$

With $\sigma = \sigma' + j\sigma''$, it can be seen that $\sigma'_{\text{intra}} \geq 0$ and $\sigma''_{\text{intra}} < 0$. The sign of σ'' is particularly important, because for $\sigma'' < 0$ (inductive surface reactance) a TM surface wave can propagate, and for $\sigma'' > 0$ (capacitive surface reactance) a TE surface wave can propagate.[7,8] The interband conductivity can be approximated analytically for low temperature,[22] although here we are interested in room temperature operation and we evaluate this contribution numerically.

B. Point source response of a graphene sheet

The Green's functions for a surface conductivity model of a graphene sheet at the interface between two dielectrics are given in Ref. 8. The electric and magnetic fields in region n of the geometry depicted in Fig. 1 are

$$\mathbf{E}^{(n)}(\mathbf{r}) = \left(k_n^2 + \nabla\nabla\cdot\right)\boldsymbol{\pi}^{(n)}(\mathbf{r}), \tag{3}$$

$$\mathbf{H}^{(n)}(\mathbf{r}) = j\omega\varepsilon_n \nabla \times \boldsymbol{\pi}^{(n)}(\mathbf{r}), \tag{4}$$

where $k_n = \omega\sqrt{\mu_n \varepsilon_n}$ and $\boldsymbol{\pi}^{(n)}(\mathbf{r})$ are the wavenumber and electric Hertzian potential in region n, respectively. Assuming that the current source $\mathbf{J}$ is in region 1, then

$$\begin{aligned}\boldsymbol{\pi}^{(1)}(\mathbf{r}) &= \boldsymbol{\pi}_1^{\mathrm{p}}(\mathbf{r}) + \boldsymbol{\pi}_1^{\mathrm{s}}(\mathbf{r}) \\ &= \int_\Omega \left\{\underline{\mathbf{g}}_1^{\mathrm{p}}(\mathbf{r},\mathbf{r}') + \underline{\mathbf{g}}_1^{\mathrm{s}}(\mathbf{r},\mathbf{r}')\right\}\cdot\frac{\mathbf{J}^{(1)}(\mathbf{r}')}{j\omega\varepsilon_1}d\Omega',\end{aligned} \tag{5}$$

$$\boldsymbol{\pi}^{(2)}(\mathbf{r}) = \boldsymbol{\pi}_2^{\mathrm{s}}(\mathbf{r}) = \int_\Omega \underline{\mathbf{g}}_2^{\mathrm{s}}(\mathbf{r},\mathbf{r}')\cdot\frac{\mathbf{J}^{(1)}(\mathbf{r}')}{j\omega\varepsilon_1}d\Omega', \tag{6}$$

where the underscore indicates a dyadic quantity, and Ω is the support of the current, and where

$$\underline{\mathbf{g}}_1^{\mathrm{p}}(\mathbf{r},\mathbf{r}') = \underline{\mathbf{I}}\frac{e^{-jk_1R}}{4\pi R} = \underline{\mathbf{I}}\frac{1}{2\pi}\int_{-\infty}^{\infty} e^{-p_1|y-y'|}\frac{H_0^{(2)}(k_\rho\rho)}{4p_1}k_\rho dk_\rho, \tag{7}$$

$$\begin{aligned}\underline{\mathbf{g}}_1^{\mathrm{s}}(\mathbf{r},\mathbf{r}') = \hat{\mathbf{y}}\hat{\mathbf{y}}g_n^{\mathrm{s}}(\mathbf{r},\mathbf{r}') + \left(\hat{\mathbf{y}}\hat{\mathbf{x}}\frac{\partial}{\partial x} + \hat{\mathbf{y}}\hat{\mathbf{z}}\frac{\partial}{\partial z}\right)g_c^{\mathrm{s}}(\mathbf{r},\mathbf{r}') \\ + (\hat{\mathbf{x}}\hat{\mathbf{x}} + \hat{z}\hat{z})g_t^{\mathrm{s}}(\mathbf{r},\mathbf{r}'),\end{aligned} \tag{8}$$

$\underline{\mathbf{I}}$ is the unit dyadic, and k_ρ is a radial wavenumber. The Sommerfeld integrals are

$$g_\beta^{\mathrm{s}}(\mathbf{r},\mathbf{r}') = \frac{1}{2\pi}\int_{-\infty}^{\infty} R_\beta \frac{H_0^{(2)}(k_\rho\rho)e^{-p_1(y+y')}}{4p_1}k_\rho dk_\rho, \tag{9}$$

where $\beta = t, n, c$, with

$$R_t = \frac{M^2p_1 - p_2 - j\sigma\omega\mu_2}{M^2p_1 + p_2 + j\sigma\omega\mu_2} = \frac{N^{\mathrm{TE}}(k_\rho,\omega)}{Z^{\mathrm{TE}}(k_\rho,\omega)}, \tag{10}$$

$$R_n = \frac{N^2p_1 - p_2 + \dfrac{\sigma p_1 p_2}{j\omega\varepsilon_1}}{N^2p_1 + p_2 + \dfrac{\sigma p_1 p_2}{j\omega\varepsilon_1}} = \frac{N^{\mathrm{TM}}(k_\rho,\omega)}{Z^{\mathrm{TM}}(k_\rho,\omega)}, \tag{11}$$

$$R_c = \frac{2p_1\left[(N^2M^2 - 1) + \dfrac{\sigma p_2 M^2}{j\omega\varepsilon_1}\right]}{Z^{\mathrm{TE}}Z^{\mathrm{TM}}}, \tag{12}$$

where $N^2 = \varepsilon_2/\varepsilon_1$, $M^2 = \mu_2/\mu_1$, $p_n^2 = k_\rho^2 - k_n^2$, $\rho = \sqrt{(x-x')^2 + (z-z')^2}$, and $R = |\mathbf{r} - \mathbf{r}'| = \sqrt{(y-y')^2 + \rho^2}$. In general, we can write $R_\beta = N_\beta/Z_\beta$.

The Green's dyadic for region 2, $\underline{\mathbf{g}}_2^{\mathrm{s}}(\mathbf{r},\mathbf{r}')$, has the same form as for region 1, although in Eq. (9) the replacement

$$R_\beta e^{-p_1(y+y')} \to T_\beta e^{p_2 y}e^{-p_1 y'} \tag{13}$$

must be made, where

$$T_t = \frac{(1+R_t)}{N^2M^2} = \frac{2p_1}{N^2Z^{TE}}, \tag{14}$$

$$T_n = \frac{p_1(1-R_n)}{p_2} = \frac{2p_1}{Z^{TM}}, \tag{15}$$

$$T_c = \frac{2p_1\left[(N^2M^2 - 1) + \dfrac{\sigma p_1}{j\omega\varepsilon_1}\right]}{N^2Z^{TE}Z^{TM}}. \tag{16}$$

In general, we can write $T_\beta = N_\beta/Z_\beta$.

Both wave parameters $p_n = \sqrt{k_\rho^2 - k_n^2}$, $n = 1, 2$, lead to branch points at $k_\rho = \pm k_n$, and thus the k_ρ-plane is a four-sheeted Riemann surface. The standard hyperbolic branch cuts[23] that separate the one proper sheet (where $\mathrm{Re}(p_n) > 0$, such that the radiation condition as $|y| \to \infty$ is satisfied) and the three improper sheets are the same as in the absence of surface conductivity σ. The zeros of the denominators, $Z^{\mathrm{TM/TE}}(k_\rho, \omega) = 0$, implicate pole singularities in the spectral plane associated with surface-wave phenomena. The four-sheeted Riemann surface for the dielectric interface case collapses to a two-sheeted Riemann surface if $k_1 = k_2$ (i.e., for a homogeneous space).

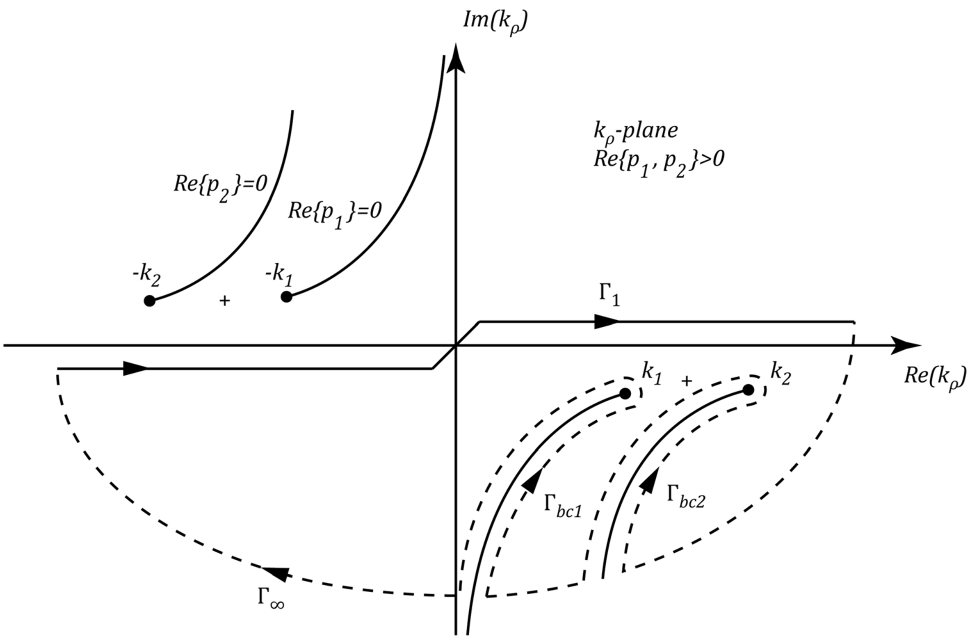

FIG. 2. Complex plane for evaluation of Sommerfeld integrals. The branch cuts are denoted by the solid hyperbolic lines, and the poles by $+$.

Using complex-plane analysis as depicted in Fig. 2, the scattered Green's function in region 1 can be written as a discrete pole (surface wave) contribution plus a branch cut integral over the continuum or radiation modes,

$$g_\beta^s(\mathbf{r},\mathbf{r}') = R_\beta^{\mathrm{res}}(\mathbf{r},\mathbf{r}') + \frac{1}{2\pi}\int_{\Gamma_{bc1}+\Gamma_{bc2}} R_\beta \frac{H_0^{(2)}(k_\rho \rho)e^{-p_1(y+y')}}{4p_1} k_\rho dk_\rho, \tag{17}$$

where

$$R_\beta^{\mathrm{res}}(\mathbf{r},\mathbf{r}') = jR'_{\beta,0}\frac{H_0^{(2)}(k_{\rho,0}\rho)e^{-p_{1,0}(y+y')}}{4p_{1,0}} k_{\rho,0}, \tag{18}$$

where R_β^{res} is the residue, $k_{\rho,0}$ is the wavenumber value at the pole, $R'_{\beta,0} = N_\beta / \left(\partial Z_\beta / \partial k_\rho\right)\big|_{k_{\rho,0}}$, and $p_{1,0} = p_1(k_{\rho,0})$. Note that unlike the case of a general multilayered medium, only one surface wave can propagate on graphene in a homogeneous medium.

Here we consider a vertical point source, which excites only TM modes. The surface-wave field can be obtained from the residue contribution of the Sommerfeld integrals. For a Hertzian dipole current $\mathbf{J}(\mathbf{r}) = \hat{\mathbf{y}}A_0\delta(x)\delta(y)\delta(z)$ the surface wave (residue) electric field in region 1 is

$$\mathbf{E}^{(1)}(y,\rho,\phi) = \frac{A_0 k_\rho^2 R'_{n,0}}{4\omega\varepsilon_1}e^{-p_1 y} \times \left\{\hat{\rho}(\phi)H_0^{(2)\prime}(k_\rho\rho) - \hat{\mathbf{y}}\frac{k_\rho}{\sqrt{k_\rho^2-k_1^2}}H_0^{(2)}(k_\rho\rho)\right\}, \tag{19}$$

where $R'_{n,0} = N^{\mathrm{TM}}(k_{\rho,0}) / \left(\partial Z^{\mathrm{TM}}(k_{\rho,0})/\partial k_{\rho,0}\right)$, $H_0^{(2)\prime}(\alpha) = \partial H_0^{(2)}(\alpha)/\partial\alpha$, $\rho = \sqrt{x^2+z^2}$, and $\hat{\rho}(\phi) = \hat{\mathbf{x}}\cos\phi + \hat{\mathbf{z}}\sin\phi$. The term $e^{-p_1 y}$ leads to exponential decay away from the graphene surface on the proper sheet (Re $(p_n) > 0$, $n = 1, 2$).

In the following, for simplicity we consider the vertical component of field, which is ϕ-symmetric, the horizontal components having explicit dependence on ϕ. At high frequency where $|k_\rho| \gg |k_{1,2}|$, $\sqrt{k_\rho^2 - k_1^2} \to k_\rho$, and for large lateral distances ($|k_\rho \rho| \gg 1$), because $H_0^{(2)'}(z) = -jH_0^{(2)}(z)$,

$$\mathbf{E}^{(1)}_{|k_\rho\rho|\gg 1}(y,\rho,\phi) = -\frac{A_0 k_\rho^2 R'_{n,0}}{4\omega\varepsilon_1}H_0^{(2)}(k_{\rho,0}\rho)e^{-p_1 y}\{j\hat{\rho}(\phi) + \hat{\mathbf{y}}\}, \tag{20}$$

and so the horizontal components have the same magnitude as the vertical component, although with a dependence on ϕ.

The total y-component of electric field in region 1 is

$$\begin{aligned} E^{(1)}(y,\rho) &= E^{\mathrm{h}} + E^{\mathrm{res}} + E^{\mathrm{bc1+bc2}} \\ &= \frac{1}{j\omega\varepsilon_1}\left(k_1^2 + \frac{\partial^2}{\partial y^2}\right)\left(\frac{e^{-jk_1R}}{4\pi R} + R_n^{\mathrm{res}}(\mathbf{r},\mathbf{r}') + \frac{1}{2\pi}\int_{\Gamma_{bc1}+\Gamma_{bc2}} R_n\frac{H_0^{(2)}(k_\rho\rho)e^{-p_1(y+y')}}{4p_1}k_\rho dk_\rho\right), \end{aligned} \tag{21}$$

where the first term is the direct source-excited field in free space (in the absence of the graphene surface), and the next two terms are the surface wave and radiation spectra, respectively. The total y-component of electric field in region 2 is

$$\begin{aligned} E^{(2)}(y,\rho) &= E^{\mathrm{res}} + E^{\mathrm{bc1+bc2}} \\ &= \frac{1}{j\omega\varepsilon_1}\left(k_2^2 + \frac{\partial^2}{\partial y^2}\right)\left(T_n^{\mathrm{res}}(\mathbf{r},\mathbf{r}') + \frac{1}{2\pi}\int_{\Gamma_{bc1}+\Gamma_{bc2}} T_n\frac{H_0^{(2)}(k_\rho\rho)e^{-p_1(y+y')}}{4p_1}k_\rho dk_\rho\right), \end{aligned} \tag{22}$$

where T_n^{res} is the residue contribution associated with the transmission coefficient. Coefficients R_n and T_n are given by Eqs. (11) and (15), respectively.

At this point some comments concerning the meaning of the continuous spectrum are appropriate. When source and observation points are in the same layer, the direct (line-of-sight) contribution E^h can be incorporated into the continuous spectrum using the integral representation (7). However, it is better to separate out this contribution, as done here, to clarify the propagation physics. To gain some understanding of the nature of the continuous spectrum in this representation, we can consider several special cases. First, assume no graphene sheet and no dielectric interface ($k_1 = k_2$). In this case there are no surface waves, and no residue contributions, $R_n = 0$, and $T_n = 1$. In the upper region $E^{(1)} = E^h$ (there is no continuous spectral contribution), and $E^{(2)}$ has only a continuous spectrum, arising from the integral in Eq. (22). Because $T_n = 1$, this integral is merely the direct (line-of-sight) radiation into the "lower" layer (e.g., compare with Eq. (7)). Thus, in this case the continuous spectrum plays no role in the upper layer, and provides the total field, which is merely the direct field, in the lower layer. If E^h were not separated out in the upper region, the continuous spectrum would provide the line-of-sight contribution in both regions.

Another case to consider is when the graphene is again removed, the lower region becomes a perfect conductor, and the upper region is lossless. In this case, the total field above the ground plane is the direct (line-of sight) term and the radiation from an image dipole (surface waves cannot propagate along a perfectly-conducting half-plane below a lossless dielectric). In this case, the continuous spectrum represents the image contribution. In short, as far as contributions to the field are concerned, when source and observation points are in the same layer, the continuous spectrum provides everything that is neither the direct term nor the surface wave, and when source and observation points are in different layers the continuous spectrum provides everything except surface waves. The continuous spectrum represents the so-called radiation modes of the structure.[24]

Finally, note that we are performing a purely proper spectral analysis in this work. In this case, complex-plane analysis on the top Riemann sheet gives the exact evaluation of the governing integrals for determining the field in terms of above-cutoff, propagating, proper surface waves and the continuous spectrum. There are no approximations made, and the integration contour never deforms onto an improper Riemann sheet. Thus, leaky modes are never implicated. In a leaky mode analysis, often done in the steepest descent (SD) plane upon which both proper and improper modes exist, one first exactly represents the integral as an integral along the SD path, plus residues associated with proper surface waves and any leaky waves captured in performing the contour deformation. Equating the two representations (from the complex wavenumber and the SD plane), the proper residues cancel and one discovers that the continuous spectrum in the wavenumber plane is equal to the integration along the SD path plus any captured leaky waves. Leaky waves approximate the continuous spectrum in a mathematically compact form in certain physical regions of space, but they are never implicated in a purely spectral wavenumber plane representation as done here. However, leaky modes can be useful as an alternative representation, and can be used to explain certain interference effects. In this regard, it can be mentioned that, as discussed below, for TM modes excited on graphene in a homogeneous medium, if $\sigma'' < 0$ the mode is on the proper sheet, whereas if $\sigma'' > 0$ the mode is on the improper sheet. Thus, in the former case the improper sheet is devoid of poles, and so there can be no leaky waves. The situation becomes more complex when the two dielectrics are not the same, and especially when a dielectric slab is involved, in which case the presence of the graphene will perturb the well-known proper, improper, and leaky modes of the slab. This is beyond the scope of the present work.

C. Surface waves guided by graphene

Surface waves supported by a graphene surface are discussed in Refs. 7 and 8. The dispersion equation for surface waves that are transverse-electric (TE) to the propagation direction ρ is

$$Z^{\mathrm{TE}}(k_\rho, \omega) = M^2 p_1 + p_2 + j\sigma\omega\mu_2 = 0, \tag{23}$$

whereas for transverse-magnetic (TM) waves,

$$Z^{\mathrm{TM}}(k_\rho, \omega) = N^2 p_1 + p_2 + \frac{\sigma p_1 p_2}{j\omega\varepsilon_1} = 0. \tag{24}$$

Letting μ_n^r and ε_n^r denote the relative material parameters of the upper and lower mediums (i.e., $\mu_n = \mu_n^r \mu_0$ and $\varepsilon_n = \varepsilon_n^r \varepsilon_0$) and $k_0^2 = \omega^2 \mu_0 \varepsilon_0$ the free-space wavenumber, then if $M = 1$ ($\mu_1^r = \mu_2^r = \mu_r$) the TE dispersion equation (23) can be solved for the radial surface-wave propagation constant, yielding

$$k_\rho^{\mathrm{TE}} = k_0 \sqrt{\mu_r \varepsilon_1^r - \left(\frac{(\varepsilon_1^r - \varepsilon_2^r)\mu_r + \sigma^2 \eta_0^2 \mu_r^2}{2\sigma\eta_0\mu_r} \right)^2}. \tag{25}$$

If, furthermore, $N = 1$ ($\varepsilon_1^r = \varepsilon_2^r = \varepsilon_r$), then Eq. (25) reduces to

$$k_\rho^{\mathrm{TE}} = k \sqrt{1 - \left(\frac{\sigma\eta}{2} \right)^2}, \tag{26}$$

where $k = k_0 \sqrt{\mu_r \varepsilon_r}$ and $\eta = \sqrt{\mu/\varepsilon}$. As discussed in Refs. 7 and 8, if $\sigma'' < 0$ (intraband conductivity dominates) the TE mode is on the improper sheet, whereas if $\sigma'' > 0$ (interband conductivity dominates) a TE surface wave on the proper sheet is obtained.

In order to obtain an analytical expression for TM waves we assume $M = N = 1$, such that

$$k_\rho^{\mathrm{TM}} = k \sqrt{1 - \left(\frac{2}{\sigma\eta} \right)^2}. \tag{27}$$

If $\sigma'' < 0$ the TM mode is a surface wave on the proper sheet, whereas if $\sigma'' > 0$ the TM mode is on the improper sheet.

The degree of confinement of the surface wave to the graphene layer can be gauged by defining a vertical attenuation length ζ, at which point the wave decays to $1/e$ of its

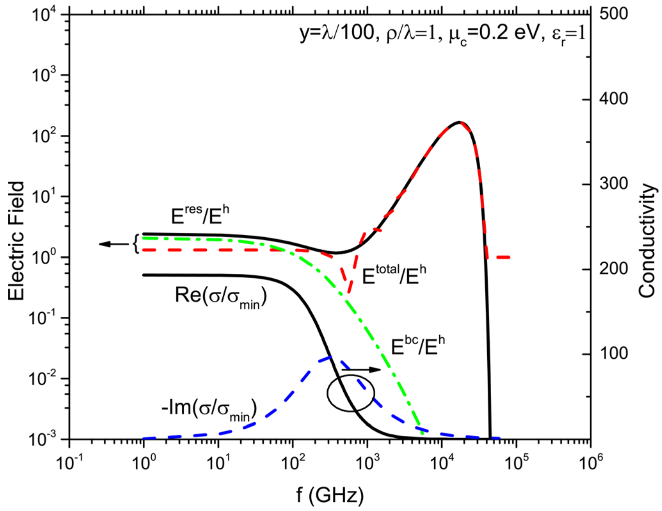

FIG. 3. (Color online) Normalized total field E^{total}/E^h, residue field E^{res}/E^h, and branch cut/continuous spectrum field E^{bc}/E^h vs frequency for $\mu_c = 0.2\,\text{eV}$. The fields are evaluated just above the graphene surface at $y = \lambda/100$ and at radial distance $\rho/\lambda = 1$.

value on the surface. For graphene embedded in a homogeneous medium characterized by ε and μ, $\zeta^{-1} = \text{Re}\ (p)$, leading to $\zeta^{\text{TE}} = 2/\sigma''\omega\mu$ $(\sigma'' > 0)$ and $\zeta^{\text{TM}} = -|\sigma|^2/2\omega\varepsilon\sigma''$ $(\sigma'' < 0)$. In most of the considered frequency range we have $\sigma'' < 0$, and so only the TM mode is excited.

III. RESULTS

In this section, the vertical electric field due to a vertical point source is shown in the far- and mid-infrared regimes. In all cases $\Gamma = 1/\tau = 1.32$ meV ($\tau = 0.5$ ps, corresponding to a mean free path of several hundred nanometers), and $T = 300\,\text{K}$. The value of the scattering rate is similar to that measured in Ref. 25 (1.1 ps), Ref. 26 (0.35 ps), and Ref. 27 (0.33 ps), where a Drude conductivity was verified in the far-infrared. In all cases the source is placed on the graphene surface $y = 0$, and the magnitude of the electric field E normalized by the vertical component of the direct field E^h (i.e., the field that would be present in the absence of the graphene surface and assuming a homogeneous dielectric) is shown.

In Fig. 3 the normalized electric field in region 1 is shown as frequency varies for chemical potential $\mu_c = 0.2\,\text{eV}$ and a vacuum background ($\varepsilon_r = \mu_r = 1$). In the considered frequency range the intraband conductivity is dominant over the interband contribution, and so $\sigma'' < 0$, such that only a TM surface wave can exist. However, above approximately 10 THz the interband term makes a non-negligible contribution to the conductivity, and must be included in the calculation. The conductivity normalized by the visible regime minimum conductivity, $\sigma_{\min} = \pi e^2/2\,h = 6.085 \times 10^{-5}$ S is also shown, and corresponds to the typical Drude behavior (2). In Fig. 3 the normalized total field E^{total}/E^h is shown, as well as the normalized residue field E^{res}/E^h and the branch cut/continuous spectrum field E^{bc}/E^h $(E^{\text{bc}} = E^{\text{bc1+bc2}}$ and $E^{\text{total}} = E^h + E^{\text{res}} + E^{\text{bc1+bc2}})$. Figure 4 shows the fields for $\mu_c = 0.5\,\text{eV}$, where in both plots the fields are evaluated just above the graphene surface at $y = \lambda/100$ and radial distance $\rho/\lambda = 1$. Figure 5 shows the normalized wavenumbers k_ρ/k and vertical confinement factors ζ/λ, where λ is the wavelength in the medium (in this case $\lambda = \lambda_0$, the free-space wavelength).

As can be seen from Fig. 5, at low frequencies the TM surface wave is poorly confined to the graphene surface ($\zeta/\lambda \gg 1$), and it is lightly damped and relatively fast (i.e., $k_\rho/k_0 \simeq 1$). For $\mu_c = 0.2\,\text{eV}$ ($\mu_c = 0.5\,\text{eV}$) the total field is smaller (larger) than the individual residue and branch cut contributions due to destructive (constructive) interference between these terms. This is also the cause of the dip near 1 THz in Fig. 3. As frequency increases into the mid-infrared, the surface wave becomes more tightly confined to the graphene layer, but becomes slower as energy is concentrated on the graphene surface. Despite this field concentration, losses do not continue to increase because the graphene surface transitions from a predominately resistive surface to a predominately reactive (inductive) surface. This is reflected in the field plots (Figs. 3 and 4); at low frequency the residue and branch

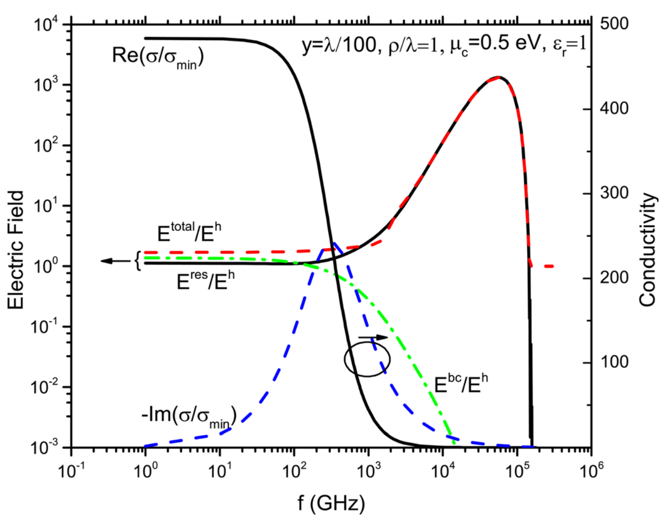

FIG. 4. (Color online) Normalized total field E^{total}/E^h, residue field E^{res}/E^h, and branch cut/continuous spectrum field E^{bc}/E^h vs frequency for $\mu_c = 0.5\,\text{eV}$. The fields are evaluated just above the graphene surface at $y = \lambda/100$ and at radial distance $\rho/\lambda = 1$.

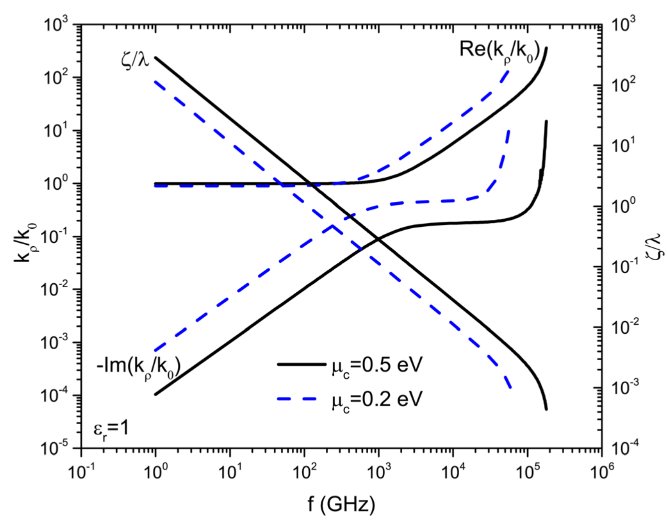

FIG. 5. (Color online) Normalized wavenumbers k_ρ/k and confinement factors ζ/λ associated with the fields in Figs. 3 and 4. Solid lines are for 0.5 eV and dashed lines are for 0.2 eV.

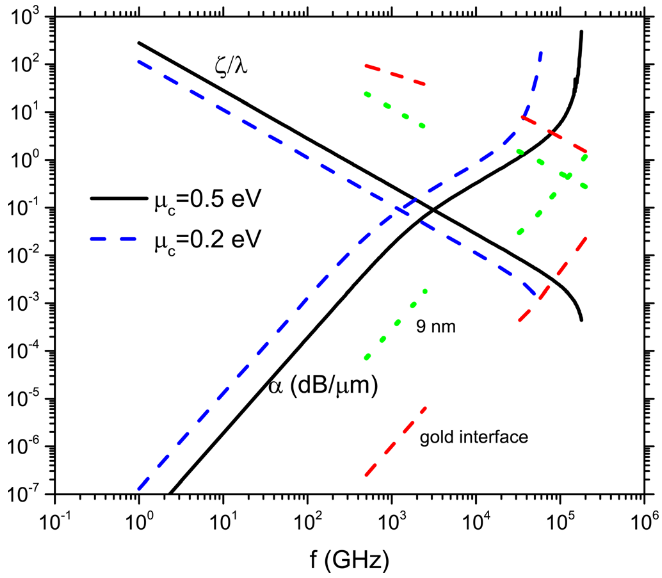

FIG. 6. (Color online) Power attenuation along the radial direction (α, dB/μm) and vertical confinement factor ζ/λ for graphene for two values of chemical potential. Also shown are results for a gold-vacuum interface and a 9 nm thickness gold film.

cut contributions are of similar magnitude but above 1 THz the branch cut contribution strongly diminishes and the total field is given approximately by the residue contribution. The strong residue component is due to the surface conductivity becoming dominated by the imaginary part, such that the TM discrete mode is weakly attenuated. For $\mu_c = 0.2\,\text{eV}$, above approximately 40 THz the residue contribution decreases sharply as the graphene surface conductivity drops and mode attenuation increases (see Fig. 5), and $E^{\text{total}} \simeq E^h$. Above approximately 80 THz the interband conductivity begins to dominate, $\sigma'' > 0$, and a TM mode is no longer excited. Because the given source does not excite a TE mode, the total field is simply the branch cut contribution (which is very small except for $\rho \ll \lambda$) and the direct field E^h. The same situation occurs for $\mu_c = 0.5\,\text{eV}$, except that the transitions occur at higher frequencies.

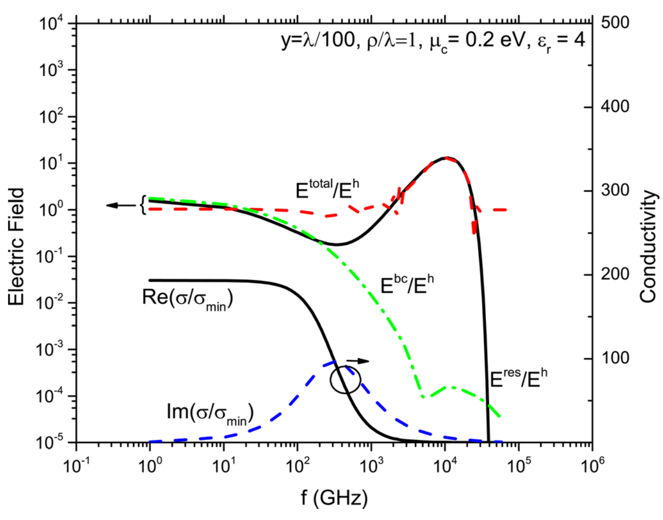

FIG. 7. (Color online) Normalized total field E^{total}/E^h, residue field E^{res}/E^h, and branch-cut/continuous spectrum field E^{bc}/E^h versus frequency for $\mu_c = 0.2$ eV and $\varepsilon_r = 4$. The fields are evaluated just above the graphene surface at $y = \lambda/100$ and at radial distance $\rho/\lambda = 1$.

Figure 6 shows the power attenuation along the radial direction, $\alpha = 8.686\ \text{Im}\ (k_\rho)$, in dB/$\mu$m, and also the vertical confinement factor ζ/λ (repeated from Fig. 5) for $\mu_c = 0.2\,\text{eV}$ and $\mu_c = 0.5\,\text{eV}$. It can be seen that in the low THz regime the mode is well-confined to the graphene surface, propagates with moderately low loss, and, from Fig. 5, is a slow wave. In contrast, if one assumes a vacuum-gold interface, then

$$k_\rho^{\text{gold}} = k_0 \sqrt{\frac{\varepsilon_r}{1+\varepsilon_r}}, \tag{28}$$

where ε_r is the complex permittivity of the metal. As an example, at 40 THz $k_\rho^{\text{gold}}/k_0 = 1 - j8.4 \times 10^{-5}$, such that the surface plasmon is very low-loss, $\alpha_{\text{gold}} = 2.4 \times 10^{-4}\,\text{dB}/\mu m$ (compared to $k_\rho^{\text{graphene}}/k_0 = 23.32 - j0.2$ and $\alpha_{\text{graphene}} = 1.38\,\text{dB}/\mu m$ for $\mu_c = 0.5\,\text{eV}$). However, the metal surface plasmon mode is very loosely- confined to the interface, $\zeta_{\text{gold}}/\lambda = 7.22$, as opposed to $\zeta_{\text{graphene}}/\lambda = 0.007$ for graphene. The results for $\zeta_{\text{gold}}/\lambda$ and α_{gold} for a gold-vacuum interface and for a 9 nm thickness gold film are also shown in Fig. 6. The conductivity was taken from measured data in Ref. 28 for the thin films, and Ref. 29 for the gold interface. The curves are not continuous because the measured data was only available in the indicated frequency ranges. It can be seen that although the attenuation is lower in the gold films and gold interface, the vertical mode confinement is much worse over the entire frequency range. It can be remarked that if one compares surface waves on graphene at 40 THz to plasmons on a gold interface in the near infrared, the graphene surface waves exhibit more loss, but better confinement. For example, at $\lambda = 1550\,\text{nm}$, $k_\rho^{\text{gold}}/k_0 = 1 - j4.2 \times 10^{-4}$, such that the surface plasmon has $\alpha_{\text{gold}} = 0.015\,\text{dB}/\mu m$ and $\zeta_{\text{gold}}/\lambda = 1.7$.

Figures 7 and 8 show the effect of changing the background permittivity to $\varepsilon_r = 4$. For this larger permittivity the field becomes more confined to the graphene sheet, and is slightly more dispersive and lossy.

Figure 9 shows the various field components versus radial distance from the source ρ, at several different frequencies. In the mid-THz range the residue field is dominant until

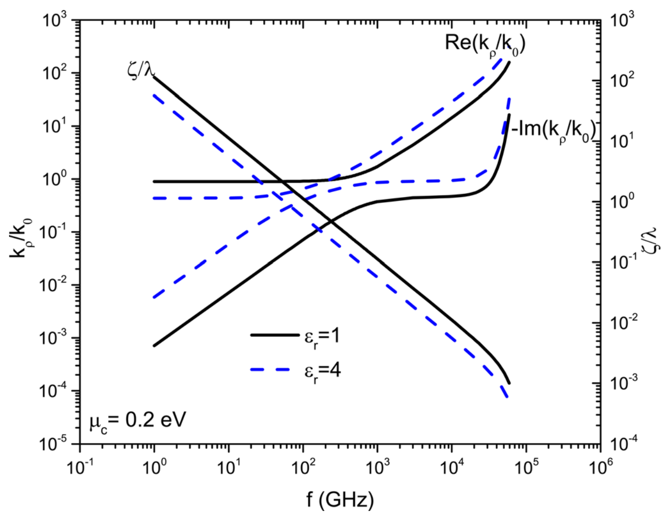

FIG. 8. (Color online) Effect on surface wavenumber k_ρ/k and mode confinement factor of background permittivity. Solid lines are for $\varepsilon_r = 1$ and dashed lines are for $\varepsilon_r = 4$.

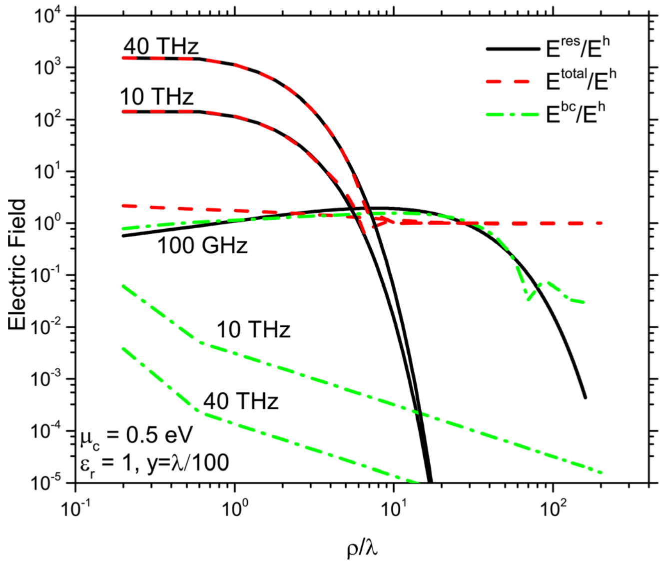

FIG. 9. (Color online) Electric field components vs radial distance along graphene sheet at three frequencies.

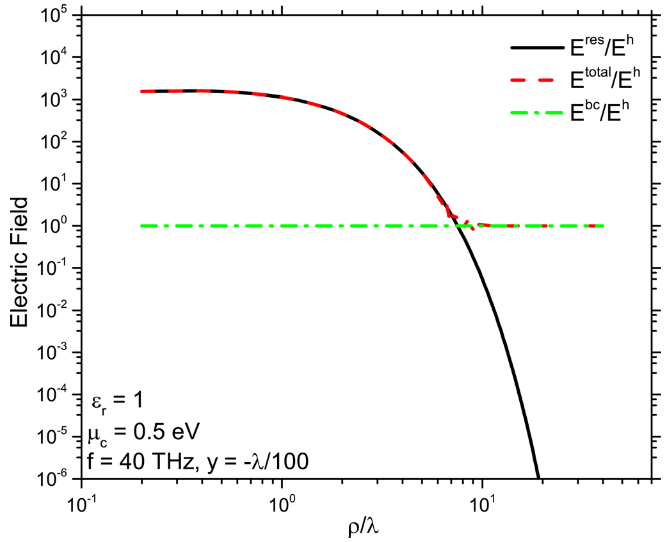

FIG. 11. (Color online) Transmitted field in region 2 (for $\varepsilon_1 = \varepsilon_2$) just under the graphene surface, at $y = -\lambda/100$, as a function of radial distance from the source ρ.

approximately $\rho/\lambda = 10$, after which point the direct field is dominant.

Figure 10 shows the various field components versus radial distance from the source ρ, at 40 THz for $\varepsilon_r = 1$ and $\varepsilon_r = 4$. Larger permittivity tends to decrease the total field due to enhanced mode attenuation.

Figure 11 shows the transmitted field in region 2 (for $\varepsilon_1 = \varepsilon_2$) just under the graphene surface, at $y = -\lambda/100$, as a function of radial distance from the source ρ. Comparing with Fig. 10, the residue and total field at $y = -\lambda/100$ are the same as at $y = \lambda/100$ (although not entirely relevant, it is worth noting that at normal incidence the plane wave transmission coefficient is $T = 1/(1 + \sigma\eta/2) = 0.9987$), but the branch cut contribution in region 2 is much larger than in region 1. This is because of the forms (5) and (6); in region 1 there is a direct field contribution associated with $\underline{\mathbf{g}}_1^{\,p}$, whereas this term is absent in region 2, and must be synthesized by the branch cut contribution.

Finally, to examine the effect of having two different permittivities, Fig. 12 shows the field in region 1 along the graphene surface as a function of radial distance from the source, ρ, for $\varepsilon_1^r = 4$ and $\varepsilon_2^r = 1$. The fields are normalized by the vertical component of the direct field E^h that would be present in the absence of the graphene surface and for a homogeneous dielectric having $\varepsilon_r = 4$. The normalized total field is now less than one because the image source (synthesized by the continuous spectrum, which is large compared to the case of $\varepsilon_1^r = \varepsilon_2^r$) produces a field that tends to cancel the original source field. This is easily shown for a simple dielectric interface in the static case using image theory.

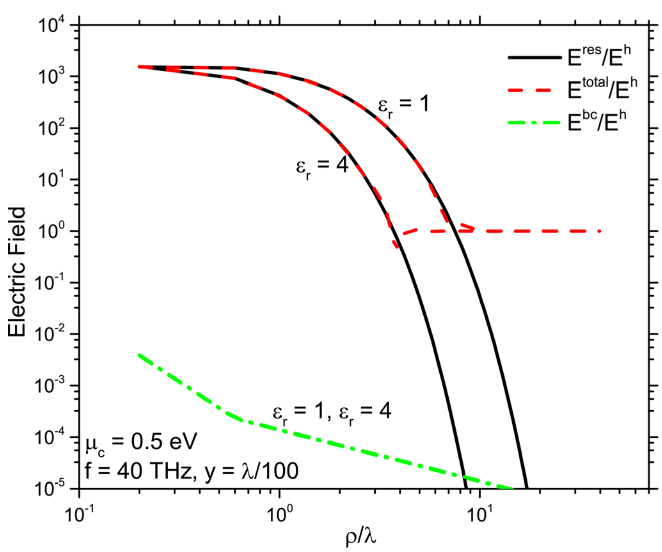

FIG. 10. (Color online) Field components at 40 THz for two different background permittivities.

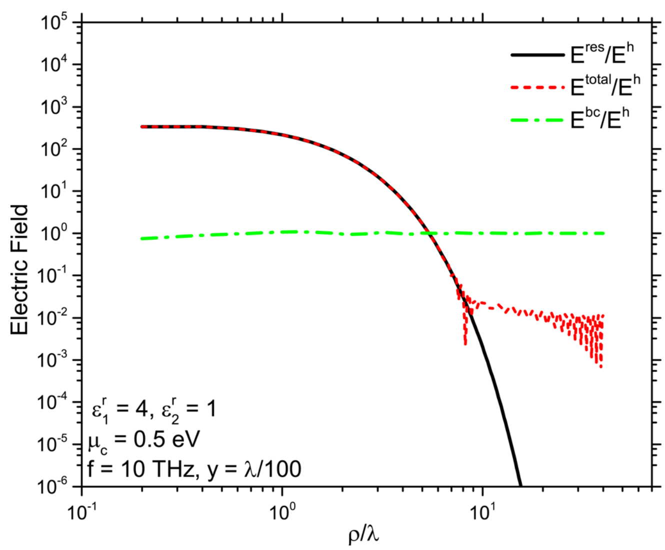

FIG. 12. (Color online) Field in region 1 along the graphene surface as a function of radial distance from the source, ρ, for $\varepsilon_1{}^r = 4$ and $\varepsilon_2{}^r = 1$. The fields are normalized by the vertical component of the direct field E^h that would be present in the absence of the graphene surface and for a homogeneous dielectric having $\varepsilon_r = 4$.

IV. CONCLUSIONS

An exact solution has been obtained for the electromagnetic field due to an electric current point source near a surface conductivity model of graphene. The field was decomposed into discrete and continuous spectral components. It has been shown that the TM discrete surface wave (surface plasmon) can dominate the response along the graphene layer in the upper GHz and low THz range, where the surface conductivity is dominated by its imaginary part. The TM surface wave propagates as a slow wave with good confinement and relatively low loss, and, in the mid-THz range, has superior propagation characteristics compared to a gold-vacuum interface.

[1]K. S. Novoselov, A. K. Geim, S. V. Morozov, D. Jiang, Y. Zhang, S. V. Dubonos, I. V. Grigorieva, and A. A. Firsov, Science **306**, 666 (2004).
[2]A. K. Geim and K. S. Novoselov, Nature Mater. **6**, 183 (2007).
[3]A. H. Castro-Neto, F. Guinea, N. M. R. Peres, K. S. Novoselov, and A. K. Geim, Rev. Mod. Phys. **81**, 109 (2009).
[4]A. Reina, X. Jia, J. Ho, D. Nezich, H. Son, V. Bulovic, M. S. Dresselhaus, and J. Kong, Nano Lett. **9**, 30 (2009).
[5]X. Li, W. Cai, J. An, S. Kim, J. Nah, D. Yang, R. Piner, A. Velamakanni, I. Jung, E. Tutuc, S. K. Banerjee, L. Colombo, and R. S. Ruoff, Science **324**, 1312 (2009).
[6]E. H. Hwang and S. D. Sarma, Phys. Rev. B **75**, 205418 (2007).
[7]S. A. Mikhailov and K. Ziegler, Phys. Rev. Lett. **99**, 016803 (2007).
[8]G. W. Hanson, J. Appl. Phys. **103**, 064302 (2008).
[9]G. W. Hanson, IEEE Trans. Antennas Propag. **56**, 747 (2008).
[10]M. Jablan, H. Buljan, and M. Soljacic, Phys. Rev. B **80**, 245435 (2009).
[11]F. Koppens, D. Chang, and J. G. de Abajo, Nano Lett. **11**, 3370 (2011).
[12]F. Rana, IEEE Trans. Nanotechnol. **7**, 91 (2008).
[13]A. Vakil and N. Engheta, Science **332**, 1291 (2011).
[14]D. R. Anderson, J. Opt. Soc. Am. B **27**, 818 (2010).
[15]E. G. Mishchenko, A. V. Shytov, and P. G. Silvestrov, Phys. Rev. Lett. **104**, 156806 (2010).
[16]G. W. Hanson, J. Appl. Phys. **104**, 084314 (2008).
[17]C. Xu, H. Li, and K. Banerjee, IEEE Trans. Electron Devices **56**, 1567 (2009).
[18]G. Deligeorgis, M. Dragoman, D. Neculoiu, D. Dragoman, G. Konstantinidis, A. Cismaru, and R. Plana, Appl. Phys. Lett. **95**, 073107 (2009).
[19]V. V. Popov, T. Y. Bagaeva, T. Otsuji, and V. Ryzhii, Phys. Rev. B **81**, 073404 (2010).
[20]M. Dragoman, D. Neculoiu, A. Cismaru, A. A. Muller, G. Deligeorgis, G. Konstantinidis, D. Dragoman, and R. Plana, Appl. Phys. Lett. **99**, 033112 (2011).
[21]V. P. Gusynin, S. G. Sharapov, and J. P. Carbotte, J. Phys. Condens. Matter **19**, 026222 (2007).
[22]V. P. Gusynin, S. G. Sharapov, and J. P. Carbotte, Phys. Rev. B **75**, 165407 (2007).
[23]A. Ishimaru, *Electromagnetic Wave Propagation, Radiation, and Scattering* (Prentice Hall, Englwood Cliffs, NJ, 1991).
[24]D. Marcuse, *Theory of Dielectric Optical Waveguides* (Academic Press, New York, 1974).
[25]Z. Q. Li, E. A. Henriksen, Z. Jiang, Z. Hao, M. C. Martin, P. Kim, H. L. Stormer, and D. N. Basov, Nature Phys. **4**, 532 (2008).
[26]C. Lee, J. Y. Kim, S. Bae, K. S. Kim, B. H. Hong, and E. J. Choi, Appl. Phys. Lett. **98**, 071905 (2011).
[27]J. Y. Kim, C. Lee, S. Bae, K. S. Kim, B. H. Hong, and E. J. Choi, Appl. Phys. Lett. **98**, 201907 (2011).
[28]M. Walther, D. G. Cooke, C. Sherstan, M. Hajar, M. R. Freeman, and F. A. Hegmann, Phys. Rev. B **76**, 125408 (2007).
[29]P. B. Johnson and R. W. Christy, Phys. Rev. B **6**, 4370 (1972).